

Pressure-induced structural, electronic, and superconducting phase transitions in $TaSe_3$

Yuhang Li(李宇航), Pei Zhou(周佩), Chi Ding(丁驰), Qing Lu(鲁清), Xiaomeng Wang(王晓梦), and Jian Sun(孙建)
Citation: Chin. Phys. B, 2024, 33 (**10**): 106102. DOI: 10.1088/1674-1056/ad6f92
Journal homepage: http://cpb.iphy.ac.cn; http://iopscience.iop.org/cpb

What follows is a list of articles you may be interested in

First-principles study of structural and electronic properties of multiferroic oxide Mn_3TeO_6 under high pressure

Xiao-Long Pan(潘小龙), Hao Wang(王豪), Lei Liu(柳雷), Xiang-Rong Chen(陈向荣), and Hua-Yun Geng(耿华运)
Chin. Phys. B, 2024, 33 (**7**): 076102. DOI: 10.1088/1674-1056/ad3ef6

Ultrafast dynamics in photo-excited Mott insulator $Sr_3Ir_2O_7$ at high pressure

Xia Yin(尹霞), Jianbo Zhang(张建波), Wang Dong(王东), Takeshi Nakagawa, Chunsheng Xia(夏春生), Caoshun Zhang(张曹顺), Weicheng Guo(郭伟程), Jun Chang(昌峻), and Yang Ding(丁阳)
Chin. Phys. B, 2024, 33 (**1**): 016103. DOI: 10.1088/1674-1056/acdc8c

Structural stability and ion migration of Li_2MnO_3 cathode material under high pressures

Ze-Ren Xie(谢泽仁), Si-Si Zhou(周思思), Bei-Bei He(贺贝贝), Huan-Wen Wang(王欢文), Yan-Sheng Gong(公衍生), Jun Jin(金俊), Xiang-Gong Zhang(张祥功), and Rui Wang(汪锐)
Chin. Phys. B, 2023, 32 (**12**): 126101. DOI: 10.1088/1674-1056/ace2b1

Prediction of superionic state in LiH_2 at conditions enroute to nuclear fusion

Fude Li(李福德), Hao Wang(王豪), Jinlong Li(李津龙), and Huayun Geng(耿华运)
Chin. Phys. B, 2023, 32 (**10**): 106103. DOI: 10.1088/1674-1056/acea68

Pressure-induced stable structures and physical properties of Sr-Ge system

Shuai Han(韩帅), Shuai Duan(段帅), Yun-Xian Liu(刘云仙), Chao Wang(王超), Xin Chen(陈欣), Hai-Rui Sun(孙海瑞), and Xiao-Bing Liu(刘晓兵)
Chin. Phys. B, 2023, 32 (**1**): 016101. DOI: 10.1088/1674-1056/ac6db5

RAPID COMMUNICATION

Pressure-induced structural, electronic, and superconducting phase transitions in $TaSe_3$

Yuhang Li(李宇航)[1], Pei Zhou(周佩)[1], Chi Ding(丁驰)[2], Qing Lu(鲁清)[2], Xiaomeng Wang(王晓梦)[1,†], and Jian Sun(孙建)[2,‡]

[1] *School of Physics, Ningxia University, Yinchuan* 750021, *China*
[2] *National Laboratory of Solid State Microstructures, School of Physics and Collaborative Innovation Center of Advanced Microstructures, Nanjing University, Nanjing* 210093, *China*

(Received 26 June 2024; revised manuscript received 14 August 2024; accepted manuscript online 15 August 2024)

$TaSe_3$ has garnered significant research interests due to its unique quasi-one-dimensional crystal structure, which gives rise to distinctive properties. Using crystal structure search and first-principles calculations, we systematically investigated the pressure-induced structural and electronic phase transitions of quasi-one-dimensional $TaSe_3$ up to 100 GPa. In addition to the ambient pressure phase ($P2_1/m$-I), we identified three high-pressure phases: $P2_1/m$-II, *Pnma*, and *Pmma*. For the $P2_1/m$-I phase, the inclusion of spin–orbit coupling (SOC) results in significant SOC splitting and changes in the band inversion characteristics. Furthermore, band structure calculations for the three high-pressure phases indicate metallic natures, and the electron localization function suggests ionic bonding between Ta and Se atoms. Our electron–phonon coupling calculations reveal a superconducting critical temperature of approximately 6.4 K for the *Pmma* phase at 100 GPa. This study provides valuable insights into the high-pressure electronic behavior of quasi-one-dimensional $TaSe_3$.

Keywords: high pressure, transition metal trichalcogenides, phase transition, superconductivity

PACS: 61.50.Ks, 61.50.Ah, 71.20.–b, 74.25.–q **DOI:** 10.1088/1674-1056/ad6f92

1. Introduction

The transition metal trichalcogenides (TMTCs) constitute a distinctive class of van der Waals (vdW) materials characterized by quasi-one-dimensional (quasi-1D) crystal structures. These materials are denoted by the general formula MX_3, where M represents a transition metal atom belonging to either group IVB (Ti, Zr, Hf) or VB (Nb, Ta), and X is a chalcogen atom from group VIA (S, Se, Te). Due to their unique quasi-1D structural characteristics, these compounds exhibit several novel electronic properties, such as variable band gaps, charge density waves (CDWs), and superconductivity.[1–9] For instance, $ZrTe_3$ is a well-known charge density wave material with a transition temperature of approximately 63 K.[6,10–12] Additionally, $TaSe_3$ exhibits superconducting transitions at temperatures around 2 K.[13–15] Moreover, TMTCs exhibit highly anisotropic optical, thermoelectric, and magnetic properties,[10,16–21] thus eliciting considerable interest among researchers in recent years. For example, with the incremental concentration of doped oxygen atoms, the thermal conductivity of quasi-1D van der Waals TiS_3 nanoribbons increases by 7.4 times.[22]

$TaSe_3$ crystallizes in a monoclinic structure under ambient pressure, with the space group $P2_1/m$. The fundamental structural unit comprises trigonal-prismatic chains aligned parallel to the b-axis, wherein each chain is composed of linearly stacked irregular prismatic cages formed by six Se atoms and a central Ta atom. Due to its unique crystal structure and diverse physical properties, including a distinctive one-dimensional chain structure, superconductivity, nontrivial topological properties, and excitonic states, $TaSe_3$ has garnered significant attention.[21,23–27] Under ambient pressure, $TaSe_3$ exhibits metallic conductivity until it reaches low temperatures, transitioning to a superconducting state at around 2 K.[14] Theoretical calculations suggest that quasi-1D $TaSe_3$ can realize multiple topological nontrivial phases under strains and is a candidate for topological superconductors.[28] Moreover, Lin *et al.* experimentally observed that $TaSe_3$ undergoes reversible strain-induced topological phase transitions from a strong topological insulator state to topologically trivial semimetal and band insulating phases, which will promote further fundamental and technical research.[29] These investigations aim to leverage topological phase transitions and its interplay with superconductivity, potentially leading to the realization of topological superconducting states.

Pressure serves as a relatively clean tuning method without introduction of additional impurity elements, offering unique advantages in exploring the correlation between structures and properties of series of TMTC materials. For example, the electronic characteristics of the highly insulating HfS_3 undergo a transition under pressure, resulting in the emergence of superconducting phases and consequent effects on the su-

†Corresponding author. E-mail: xiaomengwang@nxu.edu.cn
‡Corresponding author. E-mail: jiansun@nju.edu.cn

© 2024 Chinese Physical Society and IOP Publishing Ltd

perconducting transition temperature.[30] Additionally, theoretical calculations suggest that the semiconductor TiS_3 enters a superconducting state at approximately 80 GPa.[31] However, aside from a recent study where replacing the O atom in TaO_3 with Se atom at 300 GPa resulted in $TaSe_3$ with a T_c of 0.26 K, the investigation of the physical properties of $TaSe_3$ under high pressure has been scarcely explored.[32]

In this work, we report the discovery of high-pressure phases in $TaSe_3$ using crystal structure prediction techniques and first-principles calculations up to 100 GPa. Our results reveal that $TaSe_3$ undergoes three structural phase transitions: $P2_1/m$-I $\rightarrow$ $P2_1/m$-II $\rightarrow$ *Pnma* $\rightarrow$ *Pmma*. Among them, the difference between the high-pressure phase (labeled as $P2_1/m$-II) and ambient pressure phase (labeled as $P2_1/m$-I) is the arrangement of chains. Band-structure calculation of $P2_1/m$-I phase reveals a topological phase transition under pressure. We find that all three high pressure phases are metals, and the *Pmma* phase has a relatively strong electron–phonon coupling with an estimated T_c of approximately 6.4 K at 100 GPa.

2. Computational methods

We employed a machine-learning accelerated crystal structure prediction method MAGUS for the high-pressure crystal structure searches of $TaSe_3$.[33,34] The simulation unit contained a maximum of 48 atoms. For structure optimization and electronic structure calculations, first-principles calculations were performed using the Vienna *Ab initio* Simulation Package (VASP) with the projector augmented-wave (PAW)[35,36] method. The chosen exchange–correlation functional was the generalized gradient approximation (GGA) with the Perdew–Burke–Ernzerhof (PBE) formalism.[37] Pseudopotentials for valence electrons were set to $4s^24p^4$ for Se and $5d^36s^2$ for Ta. The energy cutoff was set to 400 eV. The Brillouin zone (BZ) sampling was meshed using the Monkhorst–Pack method with a spacing of $2\pi \times 0.025$ Å^{-1} (with the equivalent grid sizes of $4 \times 11 \times 4$ for $P2_1/m$-I, $4 \times 12 \times 3$ for $P2_1/m$-II, $6 \times 14 \times 5$ for *Pnma*, and $7 \times 14 \times 7$ for *Pmma*). Additional calculations incorporating van der Waals interactions were performed using the DFT-D2 method.[38] Atomic optimization was conducted with a force tolerance of 0.01 eV/Å. Phonon dispersions for the $P2_1/m$-II, *Pnma*, and *Pmma* structures were computed using the finite displacement method with the PHONOPY[39] program with a $2 \times 2 \times 2$ supercell. Electron–phonon coupling (EPC) calculations were carried out using density functional perturbation theory, as implemented in the Quantum-ESPRESSO code.[40] The pseudopotentials for Se and Ta were used with a kinetic energy cut-off of 150 Ry. Electron–phonon coupling was calculated by employing $2 \times 4 \times 2$ q-mesh for *Pmma* phase.

3. Results and discussion

3.1. Crystal structure search

Most TMTCs exhibit a monoclinic structure with $P2_1/m$ symmetry. However, there are some differences in their primitive unit cells, mainly in the stacking of their building blocks. Using machine-learning accelerated first-principles crystal structure prediction methods, we explored $TaSe_3$ up to 100 GPa and found three stable candidates for high-pressure phases. The first high pressure structure is identified as a new phase (SG: $P2_1/m$, $Z = 6$, labeled as $P2_1/m$-II), which has the same space group as $TaSe_3$ at ambient pressure (SG: $P2_1/m$, $Z = 4$, labeled as $P2_1/m$-I). The second structure is an orthorhombic phase (SG: *Pnma*, $Z = 4$), and the third is also an orthorhombic phase (SG: *Pmma*, $Z = 2$). As illustrated in Fig. 1(a), the calculated enthalpy and volume curves for the predicted stable phases are presented as functions of pressure, where the relative enthalpy differences ΔH are referenced to the $P2_1/m$-II phase. The enthalpy calculations suggest that the first phase transition occurs around 18.0 GPa, followed by a transition to the *Pnma* structure at approximately 42.9 GPa and finally a transition to the *Pmma* structure at around 86.1 GPa. As depicted in Fig. 1(a), the volume collapse in the transition from $P2_1/m$-I to $P2_1/m$-II is minimal, approximately 0.2%. The transition from $P2_1/m$-II to *Pnma* involves a volume collapse of approximately 2.5%, and the transition from *Pnma* to *Pmma* entails a volume collapse of about 3.9%, indicating a first-order phase transition.

The crystal structures of the $P2_1/m$-I, $P2_1/m$-II, *Pnma*, and *Pmma* are shown in Figs. 1(b)–1(e). The $P2_1/m$-II comprises three types of chains, generating the $TaSe_3$ layers oriented along the $a + c$ direction. In the subsequent high-pressure phase, characterized by the *Pnma* structure, two types of chains are present within the cell, each pair of which exhibits inversion symmetry. The third high-pressure phase, denoted as *Pmma*, exhibits a layered structure parallel to the *a*–*b* plane, with the $TaSe_3$ layer sandwiched between the Se layers. As shown in Fig. 2, phonon calculations confirmed that there are no imaginary frequencies in the entire Brillouin zone, demonstrating the dynamic stabilities of these high-pressure phases. Acknowledging the quasi-1D structural nature of $TaSe_3$ under ambient pressure, we considered the van der Waals interactions, and a set of calculations with different exchange–correlation functionals were performed. The DFT-D2 method exhibited the most favorable agreement with experimental data at ambient pressure.[41] Table 1 summarizes the optimized lattice constants at 0 GPa. Compared with the experimental values, the DFT-D2 method yielded errors of -1.03% for lattice constant a, 0.33% for b, 0.34% for c, and 0.16% for β, which are much lower than those of other functionals. The detailed structure parameters and Wyckoff positions of the three high-pressure structures are listed in Table 2.

Table 1. Calculated lattice parameters of $TaSe_3$ at 0 GPa with different exchange–correlation functionals. The values in brackets are errors compared with the experimental values. Normal GGA-PBE functional gives quite large error while the DFT-D2 method gives better results.

	a (Å)	b (Å)	c (Å)	β (°)
Expt.	10.405	3.499	9.826	106.250
DFT-D2	10.440 (0.34%)	3.511 (0.33%)	9.725 (−1.03%)	106.416 (0.16%)
DFT-D3	10.522 (1.12%)	3.485 (−0.40%)	9.882 (0.57%)	106.713 (0.44%)
DFT-D3-BJ	10.362 (−0.41%)	3.461 (−1.08%)	9.766 (−0.61%)	105.830 (−0.40%)
PBE	10.806 (3.85%)	3.530 (0.88%)	10.044 (2.22%)	107.185 (0.88%)
optB86b-vdW	10.566 (1.55%)	3.486 (−0.37%)	9.869 (0.43%)	106.444 (0.18%)
optB88-vdW	10.665 (2.50%)	3.516 (0.50%)	9.942 (1.18%)	106.531 (0.26%)
Tkatchenko–Scheffler	10.603 (1.91%)	3.486 (−0.38%)	9.937 (1.13%)	107.801 (1.46%)
DFT-ulg	10.715 (2.98%)	3.494 (−0.15%)	10.034 (2.12%)	107.853 (1.51%)
DDsC dispersion correction	10.586 (1.74%)	3.479 (−0.58%)	9.939 (1.15%)	107.180 (0.88%)

Table 2. Calculated lattice parameters, atomic coordinates and equivalent isotropic displacement parameters of the $P2_1/m$-II, *Pnma* and *Pmma* phases of $TaSe_3$ under high pressures.

Phase (pressure)	Lattice parameters (Å)			Wyckoff positions		
				x	y	z
$P2_1/m$-II (40 GPa)	$a = 8.78300$, $b = 3.17658$, $c = 13.96185$, $\beta = 106.1030°$	Ta1	2*e*	0.08908	0.75000	0.79557
		Ta2	2*e*	0.18175	0.75000	0.46341
		Ta3	2*e*	0.46137	0.75000	0.12010
		Se1	2*e*	0.04177	0.75000	0.60127
		Se2	2*e*	0.14142	0.75000	0.27035
		Se3	2*e*	0.05382	0.25000	0.92744
		Se4	2*e*	0.23137	0.25000	0.09320
		Se5	2*e*	0.27414	0.25000	0.74946
		Se6	2*e*	0.34806	0.25000	0.59045
		Se7	2*e*	0.37592	0.25000	0.42522
		Se8	2*e*	0.35617	0.75000	0.93432
		Se9	2*e*	0.43988	0.25000	0.25447
Pnma (50 GPa)	$a = 8.04898$, $b = 3.06814$, $c = 9.50369$	Ta1	4*c*	0.03529	0.25000	0.31182
		Ta2	4*c*	0.46470	0.25000	0.81182
		Se1	4*c*	0.06012	0.75000	0.10381
		Se2	4*c*	0.15207	0.25000	0.55928
		Se3	4*c*	0.22226	0.75000	0.83305
		Se4	4*c*	0.27774	0.75000	0.33305
		Se5	4*c*	0.43988	0.75000	0.60381
		Se6	4*c*	0.34793	0.25000	0.05928
Pmma (100 GPa)	$a = 5.8223$, $b = 2.89891$, $c = 5.84362$	Ta	2*f*	0.25000	0.50000	0.98569
		Se1	4*i*	0.25000	0.50000	0.52613
		Se2	4*i*	0.01418	0.00000	0.24099
		Se3	4*i*	0.48582	0.00000	0.24099

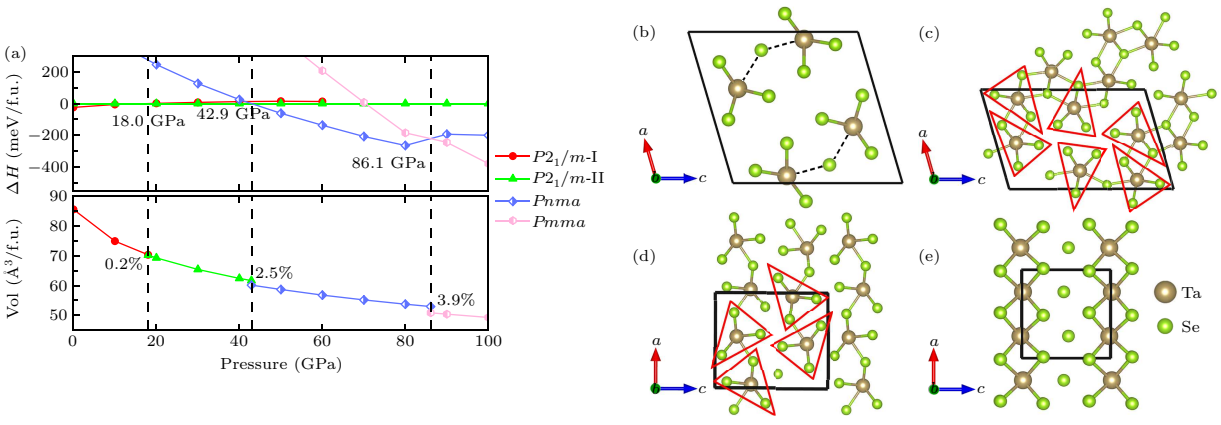


Fig. 1. Calculated enthalpy–pressure relations and volume–pressure relations of the four phases of $TaSe_3$. (a) The enthalpy differences relative to the $P2_1/m$-II and formula-unit volumes as functions of pressure. The crystal structures of the (b) monoclinic $P2_1/m$-I at 0 GPa; (c) monoclinic $P2_1/m$-II at 40 GPa; (d) orthorhombic *Pnma* at 70 GPa; and (e) orthorhombic *Pmma* phase at 100 GPa.

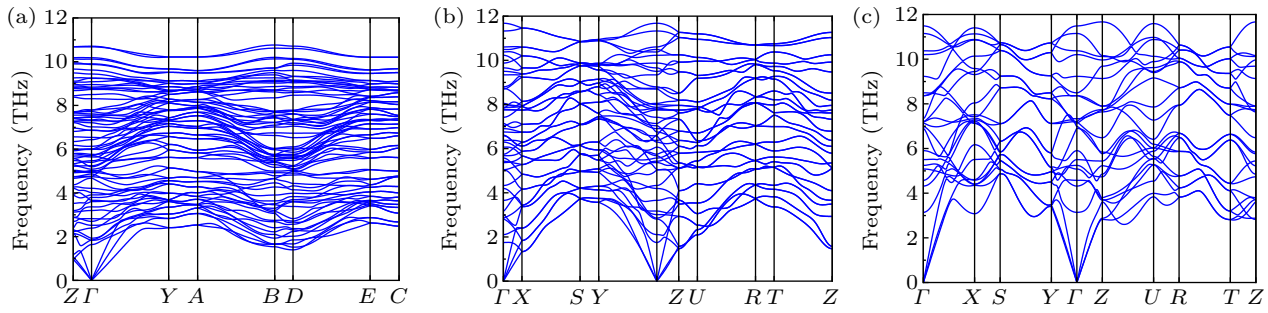


Fig. 2. The phonon spectra of (a) $P2_1/m$-II at 40 GPa, (b) *Pnma* at 70 GPa, and (c) *Pmma* at 100 GPa.

3.2. Electronic structures

We calculated the bond lengths and angle parameters of the $P2_1/m$-I phase under varying pressure conditions. As presented in Fig. 3(a), the parameters d_1–d_4 represent interchain bond lengths, while d_5–d_{10} represent intrachain bond lengths. Figures 3(b) and 3(c) illustrate that with increasing pressure, both intrachain and interchain bond lengths decrease. This phenomenon aligns with the established tendency of materials to undergo densification and tighter packing under compression. Notably, the interchain bond length d_4 demonstrates a relatively sluggish rate of decrease with increasing pressure compared to other interchain bond lengths. Conversely, the bond length d_8 within the chain exhibits a more pronounced decrease with increasing pressure compared to other intrachain bond lengths. Additionally, the changes in angle parameters with increasing pressure are depicted in Fig. 3(d).

Moreover, it is intriguing to observe how the electronic structure of the $P2_1/m$-I changes under pressure. As shown in Fig. 4, we calculated the electronic band structures and projected density of states (PDOS) for the $P2_1/m$-I structure. In the absence of spin–orbit coupling (SOC) at 0 GPa, the results of the electronic structure calculations are consistent with previous studies.[42] There are two significant band inversions along the high-symmetry paths *AB* and *DE*. Correspondingly, the band inversions near points *B* and *D* retain their intrinsic attributes and topological properties as the pressure increases. Notably, along the *DE* line, as the pressure increases to 5 GPa, the band inversion caused by Ta-d_{z^2} and Se-p_y orbitals changes to Ta-d_{z^2} and Se-p_x orbitals.

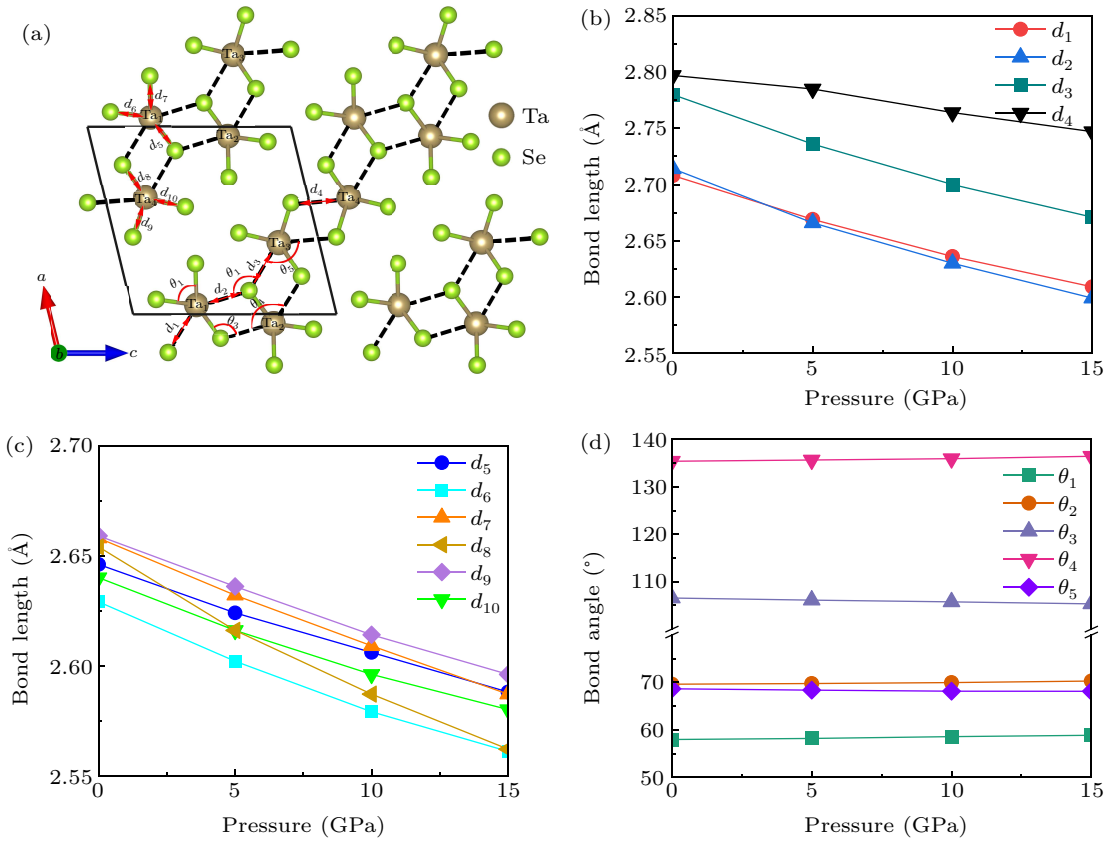


Fig. 3. (a) The illustrations of $P2_1/m$-I at 0 GPa, (b) the interchain bond lengths d_1–d_4, (c) the intrachain bond lengths d_5–d_{10}, (d) angle parameters as functions of pressure.

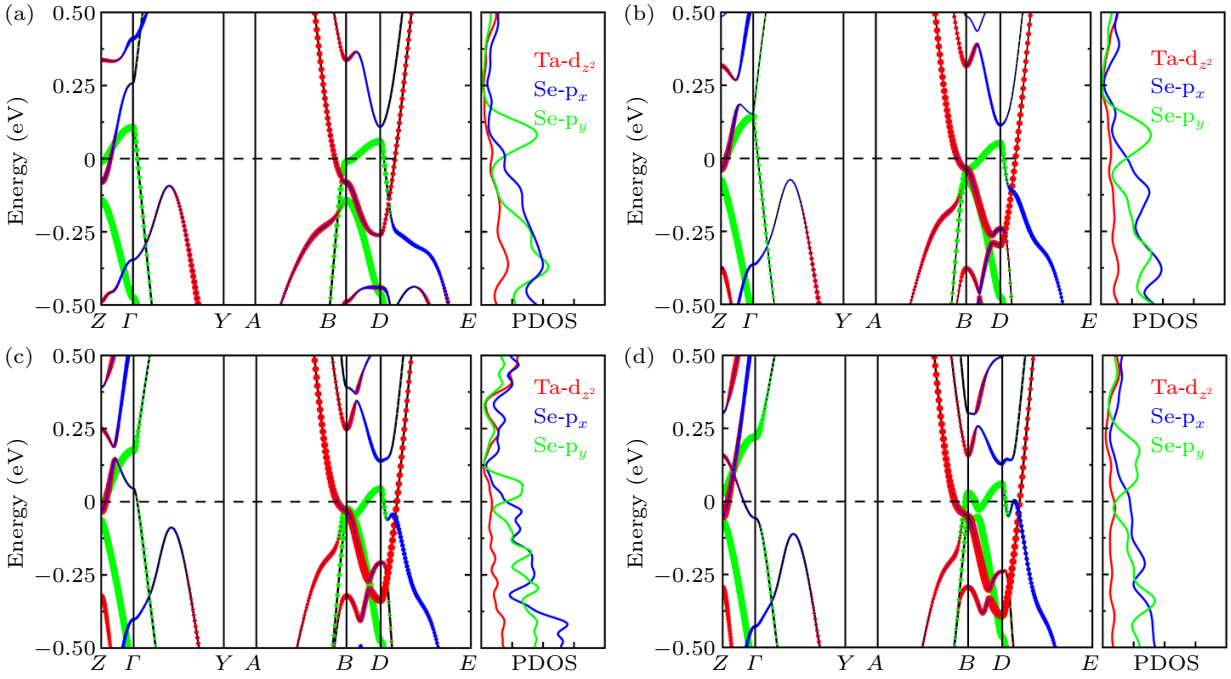


Fig. 4. Calculated electronic band structures and PDOS of the $P2_1/m$-I without SOC at (a) 0 GPa, (b) 5 GPa, (c) 10 GPa, and (d) 15 GPa.

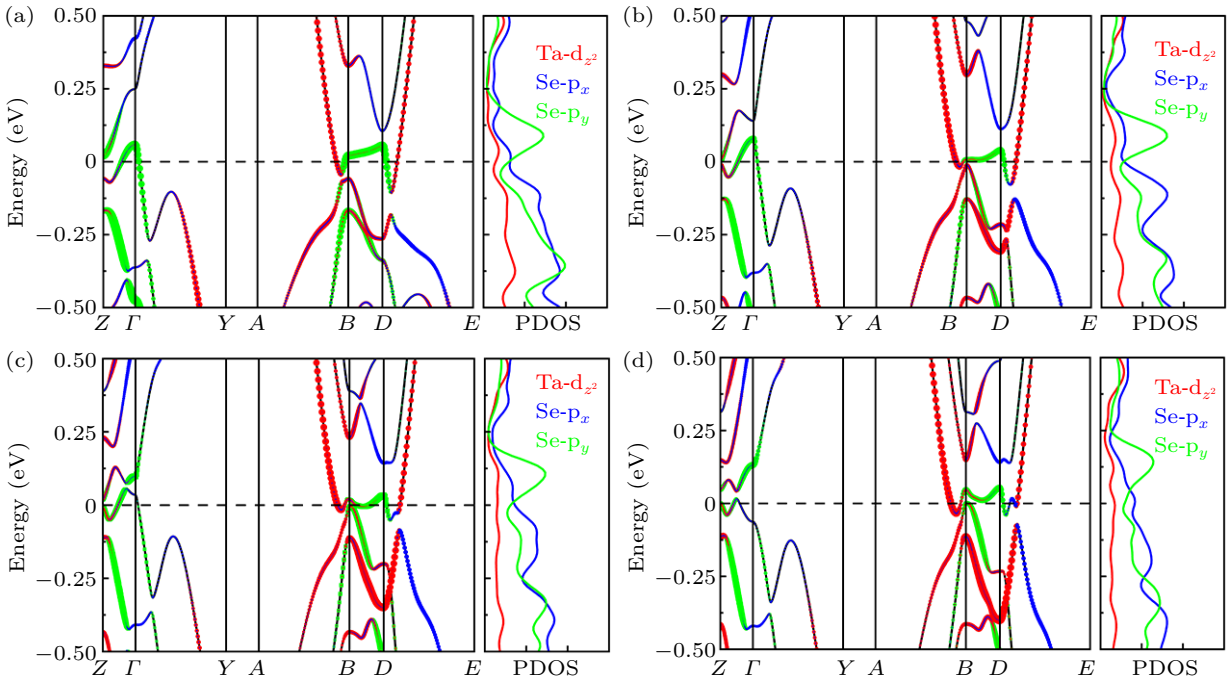


Fig. 5. Calculated electronic band structures and PDOS of the $P2_1/m$-I with SOC at (a) 0 GPa, (b) 5 GPa, (c) 10 GPa, and (d) 15 GPa.

The influence of SOC is usually significant for elements with high atomic numbers. As shown in Fig. 5, the inclusion of SOC causes a clear and prominent splitting along the *AB* and *DE* directions in the BZ. Under ambient pressure, the conduction and valence bands get inverted along the *AB* and *DE* directions near the Fermi energy. Moreover, as pressure increases, our orbital character analysis along the *DE* line indicates that the change in topological properties remains consistent with the scenario without SOC. Conversely, along the *AB* line, the energy band inversion induced by the Ta-d$_{z^2}$ and Se-p$_y$ orbitals disappears with increasing pressure, resulting in a transition from topologically nontrivial state to a trivial one.

Considering SOC, the electronic band structures and corresponding PDOS for the $P2_1/m$-II, *Pnma*, and *Pmma* structures are shown in the Figs. 6(a)–6(c). Their metallic properties are readily discernible, primarily originating from Ta-d and Se-p states near the Fermi level. Additionally, we employed the electron localization function (ELF) method to in-

vestigate the chemical bonding patterns, offering a visual representation of the bond characteristics between Ta and Se atoms. In the ELF, values of 0.5 and 1 represent free electron gas and localized electron lone pairs, respectively.[43] As illustrated in Figs. 6(d)–6(f), there is almost no electron localization between Ta and Se atoms in the $P2_1/m$-II, *Pnma*, and *Pmma* structures, indicating an ionic bonding character between Ta and Se atoms.

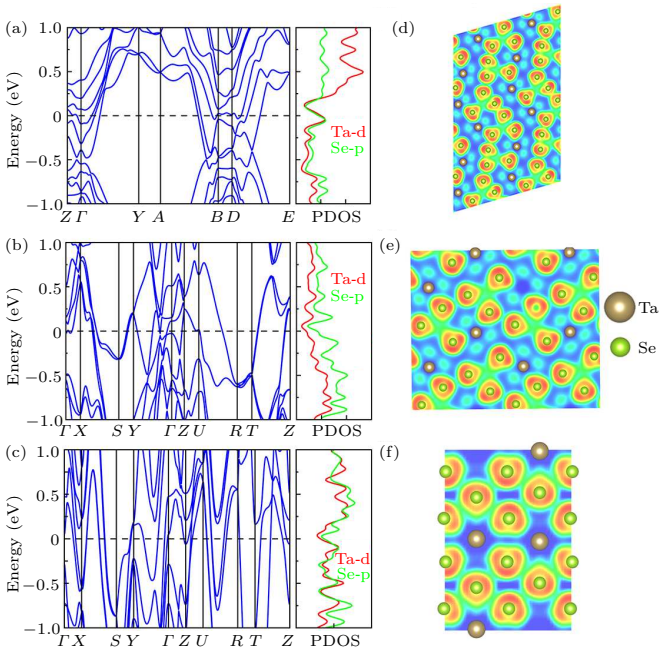


Fig. 6. Calculated electronic band structures and PDOS of the (a) $P2_1/m$-II at 40 GPa, (b) *Pnma* at 50 GPa and (c) *Pmma* at 100 GPa with SOC. ELF plots for the (d) $P2_1/m$-II at 40 GPa at the (010) plane, (e) *Pnma* at 50 GPa at the (010) plane and (f) *Pmma* at 100 GPa at the (210) plane.

3.3. Superconductivity

Since $TaSe_3$ exhibits superconductivity under ambient pressure, we investigated the potential superconductivity of the high-pressure phase *Pmma*. We utilized density functional perturbation theory to calculate the electron–phonon (e-ph) coupling, phonon spectrum, partial phonon density of states (PHDOS), Eliashberg spectral function $\alpha^2F(\omega)$, and e-ph integral $\lambda(\omega)$ at 100 GPa, as shown in the Fig. 7(a). From Fig. 7, the low-frequency phonon modes below 200 cm^{-1} are related to the hybridization of the vibrations of Ta and Se atoms, contributing 63% to the e-ph coupling parameter λ. The high-frequency modes originate from the vibrations of Se atoms.

It is worth noting that the transverse acoustic modes at the X point and the optical mode A_g ($\sim$ 100 cm^{-1}) at the Γ point soften under pressure. In these modes (see Fig. 7(b)), the vibrations of Ta atoms occur along the direction approximating the c axis with similar strength. The compressing and stretching vibrations of Se atoms at the X point are in the bc plane, while the vibrations of Se atoms at the Γ point are in the ac plane. The large phonon linewidths of these modes imply strong coupling to the electrons, playing a crucial role in contributing to the e-ph coupling parameters.

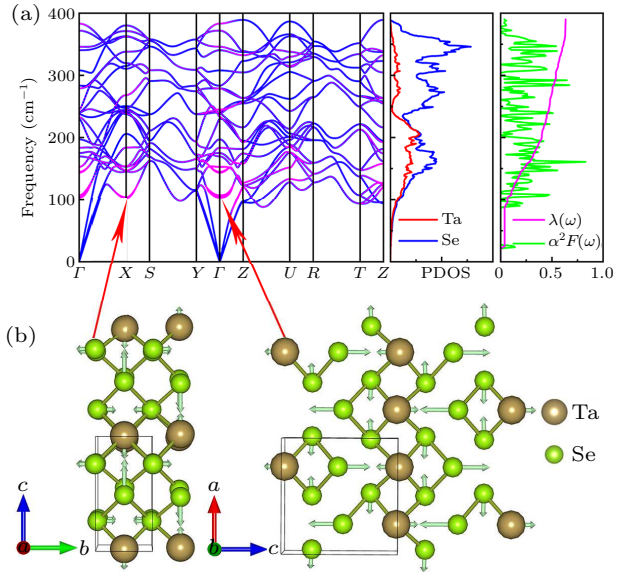


Fig. 7. (a) Phonon dispersion curves, Eliashberg spectral functions $\alpha^2F(\omega)$ together with the electron–phonon integral $\lambda(\omega)$ and phonon density of states (PHDOS) for *Pmma* of $TaSe_3$ at 100 GPa. (b) The vibrational modes of the softening modes at the X and Γ points.

Since the critical temperature (T_c) is a crucial quantity in superconductivity, we estimated T_c based on the Allen–Dynes modified McMillan equation

$$T_c = \frac{\omega_{\log}}{1.2}\exp\left[-\frac{1.04(1+\lambda)}{[\lambda-\mu^*(1+0.62\lambda)]}\right], \quad (1)$$

the Coulomb pseudopotential μ^* was set to a typical value of 0.1. The calculated critical T_c for the *Pmma* phase at 100 GPa is approximately 6.4 K, and the e-ph coupling constant λ is around 0.63.

4. Conclusion

In summary, we systematically explored the high-pressure phases of $TaSe_3$ up to 100 GPa using crystal structure prediction method MAGUS, which combines machine learning and graph theory to accelerate crystal structure searches. Employing first-principles calculations, our analysis reveals a series of structural phase transitions for $TaSe_3$. Starting from the $P2_1/m$-I phase under ambient pressure, it transforms into $P2_1/m$-II at around 18.0 GPa, then transitions to *Pnma* at approximately 42.3 GPa, and finally shifts to *Pmma* at around 86.1 GPa. For $P2_1/m$-I phase, in the absence of SOC effects, the band inversions near the B and D points persist as pressure increases. When considering SOC effects, the Brillouin zone exhibits significant SOC splitting, and at the B point, the band inversion disappears with increasing pressure, indicating a topological phase transition in $P2_1/m$-I. Band structure calculations indicate metallic natures for all three high pressure structures. ELF analysis reveals minimal electron localization between Ta and Se atoms, indicating the ionic bonding

properties. Furthermore, we performed superconducting calculations for the *Pmma* phase of $TaSe_3$, estimating a critical temperature of approximately 6.4 K at 100 GPa. These research findings represent a crucial step in understanding the structural and electronic behavior of $TaSe_3$ under high pressure, encouraging future experimental investigations into the superconductivity of $TaSe_3$.

Acknowledgments

Project supported by the National Natural Science Foundation of China (Grant Nos. 12304022 and 52361035) and the Fundamental Research Funds for the Central Universities. The calculations were carried out using supercomputers at the School of Physics at Ningxia University.

References

[1] Balandin A A, Kargar F, Salguero T T and Lake R K 2022 *Mater. Today* **55** 74
[2] Balandin AA L R and Salguero T T 2022 *Appl. Phys. Lett.* **121** 040401
[3] Brattås L K A, Krogh-Moe J, Songstad J and Pilotti Å 1972 *Acta Chem. Scand.* **26** 3441
[4] Dai J, Li M and Zeng X C 2016 *Wiley Interdiscip. Rev.-Comput. Mol. Sci.* **6** 211
[5] Zhao Q, Guo Y, Zhou Y, Yao Z, Ren Z, Bai J and Xu X 2018 *Nanoscale* **10** 3547
[6] Tsuchiya S, Matsubayashi K, Yamaya K, Takayanagi S, Tanda S and Uwatoko Y 2017 *New J. Phys.* **19** 063004
[7] Dai J and Zeng X C 2015 *Angew. Chem.-Int. Edit.* **54** 7572
[8] Kang J, Sahin H, Ozaydin H D, Senger R T and Peeters F M 2015 *Phys. Rev. B* **92** 075413
[9] Huang C, Zhang E Z, Yuan X, Wang W Y, Liu Y W, Zhang C, Ling J W, Liu S S and Xiu F X 2017 *Chin. Phys. B* **26** 067302
[10] Yue L, Xue S J, Li J R, Hu W, Barbour A, Zheng F P, Wang L C, Feng J, Wilkins S B, Mazzoli C, Comin R and Li Y 2020 *Nat. Commun.* **11** 98
[11] Zhu X D, Ning W, Li L J, Ling L S, Zhang R R, Zhang J L, Wang K F, Liu Y, Pi L, Ma Y C, Du H F, Tian M L, Sun Y P, Petrovic C and Zhang Y H 2016 *Sci. Rep.* **6** 26974
[12] Hu Y W, Zheng F P, Ren X, Feng J and Li Y 2015 *Phys. Rev. B* **91** 144502
[13] Nagata S, Kutsuzawa H, Ebisu S, Yamamura H and Taniguchi S 1989 *J. Phys. Chem. Solids* **50** 703
[14] Sambongi T M Y, Tsutsumi K, Shiozaki Y K and Yamaya Y A 1977 *J. Phys. Soc. Jpn.* **42** 1421
[15] Yamamoto M 1978 *J. Phys. Soc. Jpn.* **45** 431
[16] Island J O, Biele R, Barawi M, Clamagirand J M, Ares J R, Sanchez C, van der Zant H S J, Ferrer I J, D'Agosta R and Castellanos-Gomez A 2016 *Sci. Rep.* **6** 22214
[17] Liu H L, Yu X X, Wu K D, Gao Y, Tongay S, Javey A, Chen L D, Hong J W and Wu J Q 2020 *Nano Lett.* **20** 5221
[18] Papadopoulos N, Frisenda R, Biele R, Flores E, Ares J R, Sanchez C, van der Zant H S J, Ferrer I J, D'Agosta R and Castellanos-Gomez A 2018 *Nanoscale* **10** 12424
[19] Kezerashvili R Y and Spiridonova A 2022 *Phys. Rev. Research* **4** 033016
[20] Yu X, Wen X, Zhang W, Yang L, Wu H, Lou X, Xie Z, Liu Y and Chang H 2019 *Crystengcomm* **21** 5586
[21] Xing J, Blawat J, Speer S, Saleheen A I U, Singleton J and Jin R Y 2022 *Adv. Quantum Technol.* **5** 2200094
[22] Liu C, Wu C, Tan X Y, Tao Y, Zhang Y, Li D, Yang J, Yan Q and Chen Y 2023 *Nat. Commun.* **14** 5597
[23] Hyun J, Jeong M Y, Jung M C, *et al.* 2022 *Phys. Rev. B* **105** 115143
[24] Kargar F, Krayev A, Wurch M, Ghafouri Y, Debnath T, Wickramaratne D, Salguero T T, Lake R K, Bartels L and Balandin A A 2022 *Nanoscale* **14** 6133
[25] King P D C 2021 *Nat. Mater.* **20** 1046
[26] Liang Y, Wang J Y and Peng H L 2021 *Matter* **4** 19
[27] Ma J Z, Nie S M, Gui X, *et al.* 2022 *Nat. Mater.* **21** 423
[28] Yang X C, Luo X, Gao J J, Jiang Z Z, Wang W, Wang T Y, Si J G, Xi C Y, Song W H and Sun Y P 2021 *Phys. Rev. B* **104** 155106
[29] Lin C, Ochi M, Noguchi R, *et al.* 2021 *Nat. Mater.* **20** 1168
[30] Yue B, Zhong W, Deng W, Wen T, Wang Y, Yin Y, Shan P, Wang J T, Yu X and Hong F 2023 *J. Am. Chem. Soc.* **145** 1301
[31] Zhong X, Zhang M, Yang L, Qu X, Yang L, Yang J and Liu H 2019 *Comput. Mater. Sci.* **158** 192
[32] Li W, Li X, Zhang X, Yu H, Han F, Bergara A, Lin J, Wu J and Yang G 2023 *Physical Chemistry Chemical Physics* **25** 23502
[33] Xia K, Gao H, Liu C, Yuan J, Sun J, Wang H T and Xing D 2018 *Sci. Bull.* **63** 817
[34] Liu C, Shi J, Gao H, Wang J, Han Y, Lu X, Wang H T, Xing D and Sun J 2021 *Phys. Rev. Lett.* **126** 035701
[35] Blöchl P E 1994 *Phys. Rev. B* **50** 17953
[36] Kresse G and Furthmüller J 1996 *Comput. Mater. Sci.* **6** 15
[37] Perdew J P, Burke K and Ernzerhof M 1996 *Phys. Rev. Lett.* **77** 3865
[38] Grimme S 2006 *J. Comput. Chem.* **27** 1787
[39] Togo A, Chaput L and Tanaka I 2015 *Phys. Rev. B* **91** 094306
[40] Giannozzi P, Baroni S, Bonini N, *et al.* 2009 *J. Phys.-Condes. Matter* **21** 395502
[41] Nomura A, Yamaya K, Takayanagi S, Ichimura K, Matsuura T and Tanda S 2017 *Europhys. Lett.* **119** 17005
[42] Nie S, Xing L, Jin R, Xie W, Wang Z and Prinz F B 2018 *Phys. Rev. B* **98** 125143
[43] Becke A D and Edgecombe K E 1990 *J. Chem. Phys.* **92** 5397